

# FPO++: Efficient Encoding and Rendering of Dynamic Neural Radiance Fields by Analyzing and Enhancing Fourier PlenOctrees

Saskia Rabich, Patrick Stotko, Reinhard Klein

University of Bonn

---

## Abstract

*Fourier PlenOctrees have shown to be an efficient representation for real-time rendering of dynamic Neural Radiance Fields (NeRF). Despite its many advantages, this method suffers from artifacts introduced by the involved compression when combining it with recent state-of-the-art techniques for training the static per-frame NeRF models. In this paper, we perform an in-depth analysis of these artifacts and leverage the resulting insights to propose an improved representation. In particular, we present a novel density encoding that adapts the Fourier-based compression to the characteristics of the transfer function used by the underlying volume rendering procedure and leads to a substantial reduction of artifacts in the dynamic model. Furthermore, we show an augmentation of the training data that relaxes the periodicity assumption of the compression. We demonstrate the effectiveness of our enhanced Fourier PlenOctrees in the scope of quantitative and qualitative evaluations on synthetic and real-world scenes.*

## CCS Concepts

• *Computing methodologies* → *Image-based rendering; Visibility; Volumetric models;*

---

## 1. Introduction

Photorealistic rendering of dynamic real-world scenes such as moving persons or interactions of people with surrounding objects plays a vital role in 4D content generation and has numerous applications including augmented reality (AR) and virtual reality (VR), advertisement, or entertainment. Traditional approaches typically capture such scenarios with professional well-calibrated hardware setups [CCS\*15, GLD\*19] in a controlled environment to obtain high-fidelity reconstructions of scene geometry, material properties, and illumination. Recent advances in neural scene representations and, in particular, the seminal work in Neural Radiance Fields (NeRF) [MST\*20] marked a breakthrough towards synthesizing photorealistic novel views of complex static scenes from a set of posed multi-view images recorded by commodity cameras. Several extensions have subsequently been developed to alleviate several limitations of the original NeRF approach which led to significant reductions in the training times [MESK22] or acceleration of the rendering performance [GKJ\*21, CFHT23].

Among other approaches that explore the application of NeRF to dynamic scenarios but still suffer from slow rendering speed [GCD\*22, LCM\*22, LSZ\*22, SCL\*23], Fourier PlenOctrees (FPO) [WZL\*22] offer an efficient representation and compression of the temporally evolving scene while at the same time enabling free viewpoint rendering in real time. In particular, they join the advantages of the static PlenOctree representation [YLT\*21] with a Discrete Fourier Transform (DFT) compression technique

to compactly store time-dependent information in a sparse octree structure. Although this elegant formulation enables a high runtime performance, the Fourier-based compression results in a low-frequency approximation of the original data that is susceptible to artifacts in both the reconstructed geometry and color of the model which often persist and cannot be fully resolved even after an additional fine-tuning step. These artifacts become especially evident when recent state-of-the-art techniques are used to boost the training of the individual static neural radiance fields for each frame of the sequence and, in turn, to replace the originally applied generalizable NeRF approach [WWG\*21, WZL\*22].

In this paper, we revisit the frequency-based compression of Fourier PlenOctrees in the context of volume rendering and investigate the characteristics and behavior of the involved view-dependent color, given in form of spherical harmonics (SH) coefficients, as well as the density. Especially for the latter case of the density functions over time, our analysis reveals that they exhibit beneficial properties after the decompression that can be exploited via the implicit clipping behavior in terms of an additional Rectified Linear Unit (ReLU) operation applied for rendering that enforces non-negative values. Based on these observations, we aim to find efficient strategies that retain the compact representation of FPOs without introducing significant additional complexity or overhead while eliminating artifacts and even further accelerating the high rendering performance. To this end, we derive an efficient density encoding consisting of two transformations, where 1) a component-

dependent encoding counteracts the under-estimation of values inherent to the reconstruction with a reduced set of Fourier coefficients, and 2) a further logarithmic encoding facilitates the reconstruction from Fourier coefficients and the fine-tuning process by putting higher attention to small values in the underlying  $L_2$ -minimization. Finally, we handle artifacts at the beginning and the end of the dynamic sequence introduced by the periodic nature of the DFT basis with an augmenting method applied to the original input sequences before training.

In summary, our key contributions are:

- We perform an in-depth analysis of the compression artifacts induced in the Fourier PlenOcree representation when recent state-of-the-art techniques for training the individual per-frame NeRF models are employed.
- We introduce a novel density encoding for the Fourier-based compression that adapts to the characteristics of the transfer function in volume rendering of NeRF.
- We present an augmentation method for the training of dynamic scenes that relaxes the underlying periodicity assumption of the compression.

Our source code is available at <https://github.com/SaskiaRabich/FPOplusplus>.

## 2. Related Work

### 2.1. Neural Scene Representations

With the rise of machine learning, neural networks have become increasingly popular and attracted significant interest for reconstructing and representing scenes [SZW19, MSOC\*19, BXS\*20, NMOG20, YKM\*20, YGKL21, JMB22, SESM22]. In this context, the seminal work on NeRF [MST\*20] demonstrated impressive results for synthesizing novel views using volume rendering of density and view-dependent radiance that are optimized in an implicit neural scene representation using multi-layer perceptrons (MLP) from a set of posed images. Further work focused on addressing several of its limitations such as relaxing the dependence on accurate camera poses by jointly optimizing extrinsic [WWX\*21, LMTL21, WZML23] and intrinsic parameters [WWX\*21, WZML23], the dependence on sharp input images by a simulation of the blurring process [MLL\*22, WZML23], representing unbounded scenes [ZRSK20, BMV\*22] and large-scene environments [TCY\*22], or reducing aliasing artifacts by modeling the volumetric rendering with conical frustums instead of rays [BMT\*21, BMV\*22, BMV\*23].

### 2.2. Acceleration of NeRF Training and Rendering

A further major limitation of implicit neural scene representations is the high computational cost during both training and rendering. In order to speed up the rendering process, several techniques were proposed that reduce the amount of required samples along the ray [LMW21, NSP\*21, KNL\*22] or subdivide the scene and use smaller and faster networks for the evaluation of the individual parts [RJY\*21, RPLG21]. Some approaches represented the scene using a latent feature embedding where feature vectors are stored in voxel grids [WLB\*22, SSC22] or oc-

trees [LGZL\*20]. Another strategy for accelerating rendering relies on storing precomputed features efficiently into discrete representations such as sparse grids with a texture atlas [HSM\*21], textured polygon meshes [CFHT23], or caches [GKJ\*21] and inferring view-dependent effects by a small MLP. Furthermore, PlenOcree [YLT\*21] use a hierarchical octree structure of the density and the view-dependent radiance in terms of a SH representation to entirely avoid network evaluations.

Improving the convergence of the training process has also been investigated by using additional data such as depth maps [DLZR22] or a visual hull computed from binary foreground masks [KIT\*21] as an additional guidance. Furthermore, meta learning approaches allow for a more effective initialization compared to random weights [TMW\*21]. Similar to the advances in the rendering performance, discrete scene representations were also leveraged to boost the training. InstantNGP [MESK22] incorporated a multi-resolution hash encoding to significantly accelerate the training of neural models including NeRF. Plenoxels [FKYT\*22] stored SH and opacity values within a sparse voxel grid and TensorRF [CXG\*22] factorized dense voxel grids into multiple low-rank components. However, all the aforementioned methods and representations are limited to static scenes only and do not take dynamic scenarios like motion into account.

### 2.3. Dynamic Scene Representations

Although novel views of scenes containing motions can be directly synthesized from the individual per-frame static models, significant effort has been spent into more efficient representations for neural rendering such as subdividing the scene into static and dynamic parts [LXL\*21, WWHY20], using point clouds [WWHY20], mixtures of volumetric primitives [LSS\*21] or deformable human models [PZX\*21], or encoding the dynamics with encoder-decoder architectures [LSS\*19, MPH\*20]. Due to the success and representation power of Neural Radiance Fields, these developments also inspired recent extensions of NeRF to dynamic scenes. Some methods leveraged the additional temporal information to perform novel-view synthesis from a single video of a moving camera instead of large collections of multi-view images [PCP-MMN21, TTG\*21, LNSW21, DZY\*21, PSB\*21, GTZN21, XAS21, WCS\*22]. Among these, the reconstruction of humans also gained increasing interest where morphable [GTZN21] and implicit generative models [XAS21], pre-trained features [WWL\*21], or deformation fields [PSB\*21, WCS\*22] were employed to regularize the reconstruction. Furthermore, TöRF [ALG\*21] used time-of-flight sensor measurements as an additional source of information and DyNeRF [LSZ\*22] learned time-dependent latent codes to constrain the radiance field. Another way of handling scene dynamics is through the decomposition into separate networks where each handles a specific part such as static and dynamic content [GSKH21], rigid and non-rigid motion [WCS\*22], new areas [SCL\*23], or even only a single dynamic entity [ZLY\*21]. Similarly, some methods reconstruct the scene in a canonical volume and model motion via a separate temporal deformation field [LCM\*22, GCD\*22, FYW\*22] or residual fields [LSW\*22, WHH\*23]. Discrete grid-based representations [CXG\*22] applied for accelerating static scene training have also been extended to

factorize the 4D spacetime [CJ23, SZT\*23, IRG\*23]. In this context, Fourier PlenOctrees (FPO) [WZL\*22] relaxed the limitation of ordinary PlenOctrees [YLT\*21] to only capture static scenes in a hierarchical manner by combining it with the Fourier transform which enables handling time-variant density and SH-based radiance in an efficient way.

In this paper, we show that with an in-depth analysis of FPOs, their performance in terms of reconstruction quality and rendering speed can be significantly improved via an adaptive density encoding.

### 3. Preliminaries

In this section, we revisit the method of representing a dynamic scene using a Fourier PlenOctree [WZL\*22], which extends the model-free, static, explicit PlenOctree representation [YLT\*21] for real-time rendering of NeRFs. Given a set of  $T$  individual PlenOctrees that can be reconstructed using current state-of-the-art techniques from a dynamic sequence of  $T$  time steps, the construction of an FPO consists of two parts: 1) A structure unification of the  $T$  static models, and 2) the computation of the DFT-compressed octree leaf entries, which will be discussed in more detail in Sections 3.1 and 3.2.

In order to render an image of a scene at time step  $t$  with  $t \in \{0, \dots, T-1\}$ , the color  $\hat{\mathbf{C}}$  of a pixel is accumulated along the ray  $\mathbf{r}(\tau) = \mathbf{o} + \tau \cdot \mathbf{d} \in \mathbb{R}^3$  with origin  $\mathbf{o} \in \mathbb{R}^3$  at the camera, viewing direction  $\mathbf{d} \in \mathbb{R}^3$  as well as step length  $\tau \in \mathbb{R}_{\geq 0}$ . The ray  $\mathbf{r}$  is taken from the set of all rays  $\mathcal{R}$  cast from the input images. The accumulation is performed analogously to PlenOctrees [YLT\*21]:

$$\hat{\mathbf{C}}(\mathbf{r}, t) = \sum_{i=1}^N T_i(t) (1 - \exp(-\sigma_i(t) \delta_i)) \mathbf{c}_i(t), \quad (1)$$

where  $N$  is the number of octree leaves hit by  $\mathbf{r}$ ,  $\delta_i = \tau_{i+1} - \tau_i$  the distance between voxel borders and

$$T_i(t) = \exp\left(-\sum_{j=1}^{i-1} \sigma_j(t) \delta_j\right) \quad (2)$$

is the accumulated transmittance from the camera up to the leaf node  $i$ .

The time-dependent density  $\sigma_i(t) \in \mathbb{R}$  is reconstructed using the inverse discrete Fourier transform (IDFT) for time step  $t$  applied to the values stored in the FPO. Similarly, the time- and view-dependent color  $\mathbf{c}_i(t) \in \mathbb{R}^3$  is obtained by first applying the IDFT to the FPO entries of the respective SH-coefficients  $\mathbf{z}_i(t) \in \mathbb{R}^{Z \times 3}$  with  $Z$  SH-coefficients per color channel, and then querying  $\mathbf{z}_i(t)$  for the given viewing direction  $\mathbf{d}$ . Finally, the sigmoid function is applied to  $\mathbf{c}_i(t)$  for normalization. In the following, we omit the subscript  $i$  for brevity as all computations are performed per leaf. Since all operations are differentiable with respect to the octree leaves, the compressed representation can be directly fine-tuned based on the rendered images using the following loss function [WZL\*22]:

$$\mathcal{L} = \sum_{t=0}^{T-1} \sum_{\mathbf{r} \in \mathcal{R}} \|\mathbf{C}(\mathbf{r}, t) - \hat{\mathbf{C}}(\mathbf{r}, t)\|_2^2. \quad (3)$$

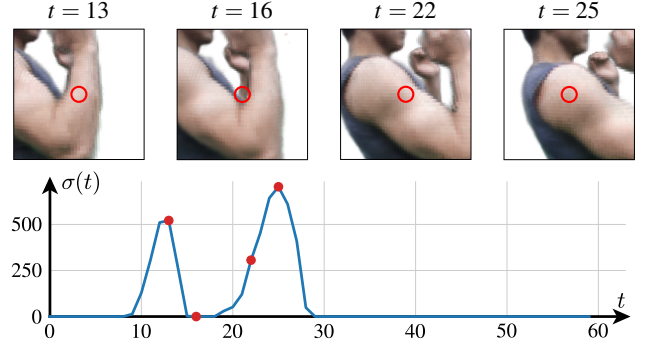


Figure 1: Density over time of a single octree leaf. The leaf is marked in red in the respective images taken from the same view at different time steps  $t$ . Although the opacity is similar in the views, highly varying density are observed over time, except for  $t = 16$  where there is empty space in the tree leaf.

#### 3.1. PlenOctree Structure Unification

To construct an FPO, time-dependent SH coefficients and densities from all PlenOctrees are merged into a single data structure. The sparse octree structures are first unified to obtain the structure of the FPO. This unification can be performed by finding every position with a PlenOctree leaf with maximum depth, which are the leaves containing information about the scene content in at least one time step, and then refining all PlenOctrees to have the same structure with leaves of maximum depth at these positions [WZL\*22].

#### 3.2. Time-variant Data Compression

After creating the structure of the FPO, the SH coefficients and densities of all leaves and time steps are compressed by converting them into the frequency domain using the DFT. Each SH coefficient and density value is compressed independently in each octree leaf, where only  $K_\sigma$  components for the transformed density functions and  $K_z$  components for the SH coefficients are kept and stored. Thereby,  $K$  components correspond to  $0.5 \cdot (K+1)$  frequencies as the Fourier representation is split into its real and imaginary parts. Omitted components correspond to higher frequencies in the frequency domain, so a low-frequency approximation of the data is computed. Thus, the entries of the Fourier PlenOctree are calculated as

$$\omega_k = \sum_{t=0}^{T-1} x(t) \cdot \text{DFT}_k(t) \quad (4)$$

with

$$\text{DFT}_k(t) = \begin{cases} \frac{1}{T} \cos\left(\frac{k\pi}{T}t\right) & \text{if } k \text{ is even,} \\ \frac{1}{T} \sin\left(\frac{(k+1)\pi}{T}t\right) & \text{if } k \text{ is odd.} \end{cases} \quad (5)$$

Here,  $x$  represents either the density  $\sigma$  or a component of the SH coefficients  $\mathbf{z}$ , and  $\omega_k$  is the  $k$ -th Fourier coefficient for the density or the specific SH coefficient. For rendering, which remains completely differentiable, the time-dependent densities and SH co-

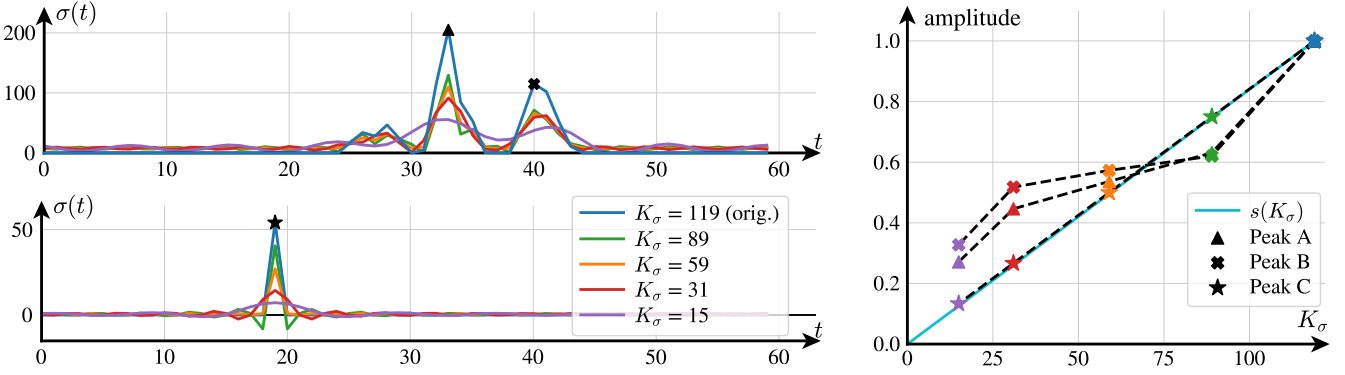


Figure 2: Two exemplary density functions over time (left) reconstructed with different number of coefficients  $K_\sigma$ . The original function of  $T$  time steps is equal to its reconstruction with  $K_\sigma = 119$  Fourier coefficients. The falloff of the marked peaks relative to its original value (right) is depending on  $K_\sigma$  and follows the linear scaling function  $s(K_\sigma)$ .

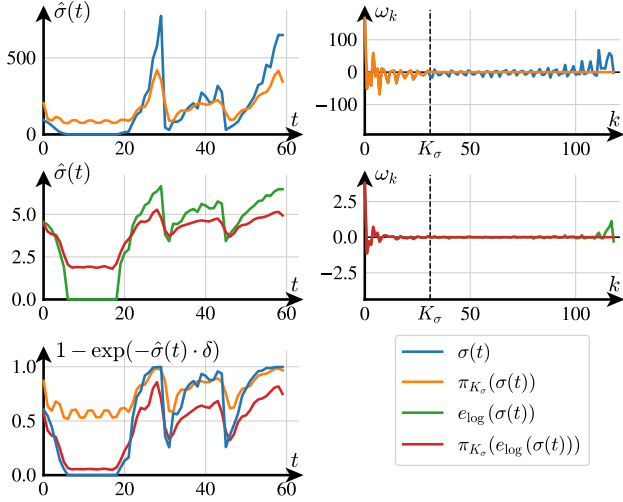


Figure 3: A density function and its reconstruction  $\pi_{K_\sigma}$  using the DFT and IDFT with  $K_\sigma = 31$  (top left) and the same function and its reconstruction after applying our logarithmic encoding  $e_{\log}$  (center left). Their full and compressed Fourier representations (top and center right) show that a logarithmically scaled function contains less high-frequency information that gets lost during compression. Applying the transfer function to the reconstructions (bottom left) shows that the logarithmic version can better represent the original function.

efficients can be reconstructed using the IDFT:

$$x(t) = \sum_{k=0}^{K-1} \omega_k \cdot \text{IDFT}_k(t) \quad (6)$$

with

$$\text{IDFT}_k(t) = \begin{cases} \cos\left(\frac{k\pi}{T}t\right) & \text{if } k \text{ is even,} \\ \sin\left(\frac{(k+1)\pi}{T}t\right) & \text{if } k \text{ is odd.} \end{cases} \quad (7)$$

#### 4. FPO Analysis

Upon investigation of the FPO representations of a dynamic scene, we especially notice geometric reconstruction errors that are visible as ghosting artifacts of scene parts from other time steps. While the DFT in general is able to represent arbitrary discrete sequences using  $K = 2T - 1$  Fourier coefficients, we observe that cutting off high frequencies for the purpose of compression leads to artifacts that are equally distributed across the entire signal. These artifacts persist even after fine-tuning which implies that the lower-dimensional representation of the signal cannot capture the crucial characteristics of the original values at each time step from the static reconstructions. However, especially the density functions always exhibit the same properties, that upon analysis lead to two key observations.

When dealing with static PlenOctrees that have been optimized independently, it is possible that leaf entries are highly varying, even though the rendered results are similar. This is due to the use of the exponential function in Eq. 1 and 2 to compute the density and transmittance given the  $\sigma$  values or in case of the color values the application of the sigmoid function after evaluating the SH coefficients. For large input values, both of these functions saturate, which, especially for the density, can lead to large differences where scene content appears similarly opaque, as shown in Fig. 1.

Compressing a time-dependent function with a reduced amount of frequencies in Fourier space returns a smoothed approximation of the original function. Fig. 2 shows this effect for different settings of the number of components  $K_\sigma$  used to represent the signal. Fewer frequencies thereby result in smoother functions and higher reconstruction error, especially visible with sharp peaks. The approximation error is similar for all densities in that values with a higher absolute difference to the average  $\bar{\sigma} = 1/T \sum_{t=0}^{T-1} \sigma(t)$  are also reconstructed with higher error. However, large positive values do not need to be reconstructed as precisely as smaller values or zero-densities, which represent transparent and semi-opaque surfaces, or empty space, respectively. The saturation property of the transfer function allows for higher reconstruction errors of large positive values, which is visualized in Fig. 3. Smoothing the function by applying for instance a logarithmic function can increase



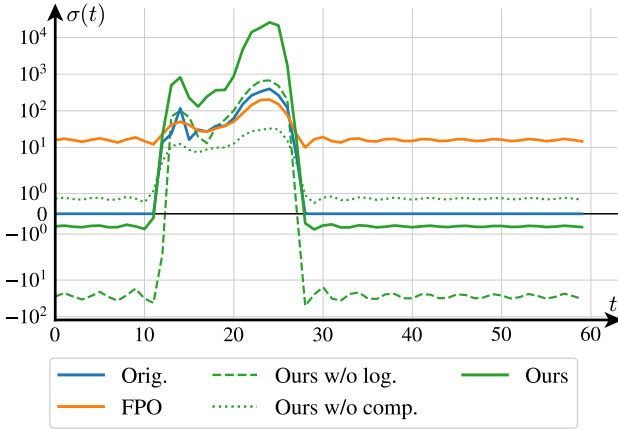


Figure 4: Impact of different encodings to the DFT compression of FPOs of the density values on the quality of the reconstruction. Our approach applies component-dependent (comp.) and logarithmic (log.) encoding on top of the DFT and IDFT for the respective plots.

the reconstruction capabilities of the Fourier compression as less high-frequent information is present in the signal which could be lost through compression.

Not only the IDFT with fewer frequencies focuses the approximation of all input values equally, in a similar way this also applies to the fine-tuning process. The  $L_2$ -minimization tries to improve the reconstruction with equal focus on all values, while this is not necessary for large densities in opaque areas. This generally leads to the conclusion that the focus of the density reconstruction needs to be concentrated on smaller values and zero-density areas.

During rendering an FPO, zero-densities are interpreted as free space and color computations are skipped for these locations. Negative densities generally cannot be interpreted in a meaningful way. However, during rendering and fine-tuning, colors only need to be evaluated for existing geometry, that is for positive densities, so that negative values can also be used to represent free space. In general, this implicit clipping via the ReLU function lifts the restriction that free space has to be represented as a zero-value and grants more freedom to the representation of zero-density values and, thus, also to the DFT approximation.

## 5. Method

### 5.1. Density Encoding

Based on the insights of the aforementioned analysis, we propose an encoding for the densities to facilitate the reconstruction of the original  $\sigma$ . During the FPO construction, we perform the compression on encoded densities

$$\sigma' = e_{\text{comp}}(e_{\text{log}}(\sigma)) \quad (8)$$

where the encoding consists of a component-dependent and a logarithmic part. We use the latter also during rendering and fine-tuning the FPO, while we apply the former only as an initialization during construction.

Fig. 4 shows the differences in the reconstruction of a density function using both or only one part of the encoding. The encoding allows for a better reconstruction of the original densities without any fine-tuning than can be achieved with only the DFT and IDFT.

#### 5.1.1. Component-dependent Encoding

With the DFT, a smoothed version of the original function is reconstructed, where low  $\sigma$  values are increased, while high  $\sigma$  values are reduced. This leads to an under-estimation of its variations over time.

Intuitively, using fewer components leads to this under-estimation as fewer frequencies are summed up to reconstruct the original function. The heights of the peaks in the function are correlated with the ratio

$$s(K_\sigma) = 0.5 \cdot (K_\sigma + 1) / T \quad (9)$$

between the number of frequencies  $K_\sigma$  and the number of time steps  $T$ , as shown in Fig. 2. Amplitudes of the density function are, however, not smaller compared to zero but relative to the average  $\bar{\sigma}$ . Smaller than average values thus need to be scaled in the opposite direction.

We shift the densities by  $\sigma_{\text{shift}}$  and then scale them with the inverse ratio  $1/s(K_\sigma)$  before the DFT during FPO construction for a better approximation:

$$e_{\text{comp}}(\sigma) = \frac{1}{s(K_\sigma)} \cdot (\sigma - \sigma_{\text{shift}}) + \sigma_{\text{shift}} \quad (10)$$

$$\sigma_{\text{shift}} = \begin{cases} \bar{\sigma} & \text{if } \exists t \in \{0, \dots, T-1\}: \sigma(t) = 0, \\ 0 & \text{otherwise.} \end{cases} \quad (11)$$

In octree leaves that only contain positive  $\sigma$  for all  $t$ , applying  $e_{\text{comp}}$  with a shift by the mean value  $\bar{\sigma}$  can lead to undesired non-positive values, where positive  $\sigma$  can be accidentally pushed below zero and cause holes in the reconstructed model. Thus, the shifting is only applied if empty space and, in turn, at least one zero-density is encountered.

This scaling can lead to higher amplitudes in the reconstruction than desired. However, this is not problematic following the two key observations: both large and small values can be larger or smaller, respectively, to achieve the same result. We can largely remove geometric artifacts from incorrectly reconstructed zero-values using this technique. The effect of the scaling is shown in Fig. 4. We apply  $e_{\text{comp}}$  only during FPO construction for a better initialization of the Fourier components in the octree leaves, so its inverse and the involved values of  $\bar{\sigma}$  do not have to be used and stored for rendering or fine-tuning. Since the component-dependent encoding introduces negative densities, it needs to be applied after  $e_{\text{log}}$ .

#### 5.1.2. Logarithmic Density Encoding

We use the observation that high density values can have a larger approximation error without impairing the rendered result to improve the reconstruction with the IDFT. To weigh the values according to their importance in reconstruction and focus the approximation on densities near or equal to zero, larger values should be

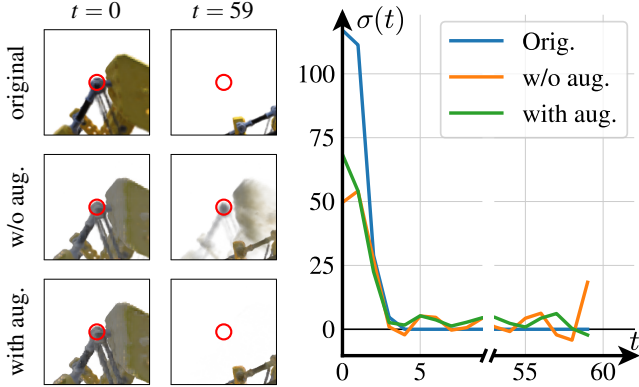


Figure 5: Impact of the time step augmentation on the reconstruction of the density values for the reconstructed  $T = 60$  time steps. Additional time steps at the start and end are omitted. Logarithmic and component-dependent encoding are additionally applied in the renderings to only show the artifacts induced by the periodicity assumption.

mapped closer together, while smaller values should stay almost the same.

This property is satisfied when encoding the individual non-negative density values  $\sigma$  logarithmically using

$$e_{\log}(\sigma) = \log(\sigma + 1) \quad (12)$$

before applying the DFT. We choose the shift by 1 so that  $e_{\log}$  remains a non-negative function for non-negative input densities with  $e_{\log}(0) = 0$ . During rendering, we apply the inverse of Eq. 12 after the IDFT to project the densities back to their original range. The effect of this encoding can be seen in Fig. 4. The encoded density sequences are smoother and thus easier to approximate with a low-frequency Fourier basis. Furthermore, the  $L_2$ -error in fine-tuning is smaller for encoded high values than without scaling, and we focus the optimization on the more important parts of the reconstruction.

## 5.2. Data Augmentation

The DFT uses periodic functions to reconstruct a discrete function and therefore induces periodicity into the reconstruction. If  $T$  time steps  $t \in \{0, \dots, T-1\}$  are given, querying the DFT for  $t = T$  thus returns the value for  $t = 0$ . Arbitrary movements can introduce large jumps in the density function from the last to the first time step, which are harder to approximate and lead to artifacts, as depicted in Fig. 5. They are difficult to resolve during fine-tuning and have a large impact on the quality of the reconstruction.

While the artifacts cannot be removed completely from the reconstruction, the respective time steps can be cropped out from rendering. Therefore, we propose to augment the input data by copying the respective first and last time step so that we can crop the additional time steps during rendering and improve the reconstruction. Then, we perform the DFT with  $T+2$  time steps, where the data of  $t' = 0$  and  $t' = 1$ , as well as  $t' = T$  and  $t' = T+1$  are equal, respectively. During rendering we shift  $t$  to the correct time step

before querying the IDFT. The effect of the augmentation is visualized in Fig. 5. Without augmentation, the peak at the start of the sequence influences the reconstruction at the last time steps significantly, which is counteracted by the augmentation.

## 6. Experimental Results

### 6.1. Datasets

We use synthetic data sets of the *Lego* scene from the NeRF synthetic data set [MST\*20] and from a walking human model (*Walk*) generated from motion data from the CMU Motion Capture Database [CMU22] using a human model [Mak22]. Each data set includes 125 inward-facing camera views with a resolution of  $800 \times 800$  pixels per time step anchored to the model, where 20% are used for testing purposes. The real-world NHR data sets *Basketball*, *Sport 1*, *Sport 2* and *Sport 3* including corresponding masks [WWHY20] are used for evaluation on real scenes. *Basketball* includes 72 views of  $1024 \times 768$  and  $1224 \times 1024$  resolution, where 7 views are withheld for testing purposes, whereas the *Sport* data sets each contain 56 views with 6 views withheld for testing. We evaluate our approach against the reimplementation of the baseline method of Fourier PlenOctrees [WZL\*22].

### 6.2. Training

To obtain the static PlenOctrees, a set of  $T = 60$  NeRF-models is trained first. The networks use the multiresolution hash encoding and NeRF network architecture of Instant-NGP [MESK22] but produce view-independent SH coefficients instead of view-dependent RGB colors as output, analogous to NeRF-SH [YLT\*21]. Training is performed incrementally, similar to the idea of INV [WSR\*23], where 4 key frames are selected equidistantly, and subsequent time steps are trained for a shorter amount of time after being initialized from models of previous time steps. Rays are chosen from training images with importance sampling, adopting the idea from DyNeRF [LSZ\*22], to focus the training of subsequent time steps on scene content and its changes. The training images are scaled down by a factor of two.

The PlenOctrees are extracted from the trained implicit reconstructions [YLT\*21] using 9 SH coefficients per color channel on a grid of size  $512^3$ . Instead of choosing bounds for each PlenOctree that cover the whole movement, the bounds of each PlenOctree are kept constant over time with centers at different positions. This allows for shifting the different time step to the same position and enclose the scene in a much tighter bounding box, which enables representing larger motions, such as a walking human. When rendering the FPO, the inverse shift is applied to show the scene content at the correct position. Fine-tuning of the static PlenOctrees is performed for 5 epochs with training images at full resolution.

We choose the same parameters for the Fourier approximation as in the original approach [WZL\*22]: For the density,  $K_{\sigma} = 31$  Fourier coefficients are stored in the FPO while  $K_z = 5$  components are used for the SH coefficients of each color channel. For fine-tuning, the training data of all time steps is randomized and used for optimization each epoch at full resolution. The augmented time steps are not fine-tuned explicitly with training data as they serve as



Figure 6: Renderings of FPOs of different dynamic scenes without and with logarithmic and component-dependent encoding and additional time step augmentation after 10 epochs of fine-tuning.

Table 1: Comparison of achieved metrics averaged over all data sets with different combinations of logarithmic encoding (log.), component-dependent encoding (comp.) and time step augmentation (aug.), both before and after fine-tuning for 1 and 10 epochs. Arrows indicate whether a high value ( $\uparrow$ ) or a low value ( $\downarrow$ ) is better. Best and second best results are marked in green and yellow, respectively.

Fine-tuning	0 epochs			1 epoch			10 epochs		
	PSNR $\uparrow$	SSIM $\uparrow$	LPIPS $\downarrow$	PSNR $\uparrow$	SSIM $\uparrow$	LPIPS $\downarrow$	PSNR $\uparrow$	SSIM $\uparrow$	LPIPS $\downarrow$
FPO	17.453	0.890	0.180	21.453	0.917	0.149	23.631	0.920	0.131
Ours w/o comp.	23.018	0.926	0.123	29.591	0.950	0.097	30.849	0.957	0.092
Ours w/o log.	23.452	0.915	0.131	25.980	0.934	0.111	27.495	0.938	0.108
Ours	23.739	0.908	0.118	28.627	0.939	0.100	29.761	0.947	0.099
Ours with aug.	23.711	0.908	0.118	28.577	0.938	0.099	29.712	0.946	0.099

a buffer between adjacent time steps and are excluded from rendering. All training is performed on NVIDIA GeForce RTX 3090 and 4090 GPUs, where frame rates and training times are listed here for the 3090 GPU.

### 6.3. Evaluation

Fig. 6 shows renderings of the original and our enhanced FPO. In comparison to the standard FPO, the amount of artifacts from geometry of other time steps that were visible as floating structures is significantly reduced. In the case of fast moving scene content such as the legs in the *Walk* scene, artifacts are mostly removed and much much less apparent. Even without fine-tuning, the geometry is reconstructed well, as can be seen in Fig. 7.

In the enhanced FPO before fine-tuning, gray artifacts are still visible on the reconstruction. These stem from approximation errors in the SH coefficient functions, which are not altered by our

approach. Leaves that are empty most of the time contain a default value of zero in most static PlenOctrees, which result in the gray coloration. The fine-tuning process however ensures a realistic reconstruction of RGB colors for all time steps.

Tab. 1 gives an overview of the achieved PSNR, SSIM [WBSS04] and LPIPS [ZIE\*18] values. While our approach still requires some fine-tuning to improve the view-dependent appearance, a much better result can be achieved in only a single epoch of fine-tuning than the baseline FPO achieves with ten times the amount of optimization time. A single epoch of fine-tuning requires up to an hour for the real-world data sets with fewer images. Even without further optimization, the modified FPO achieves higher metrics than the original FPO due to a better initialization of the geometry. Due to this fact, the creation process of an FPO representation of a dynamic scene is accelerated indirectly, as fewer time needs to be spent on fine-tuning.



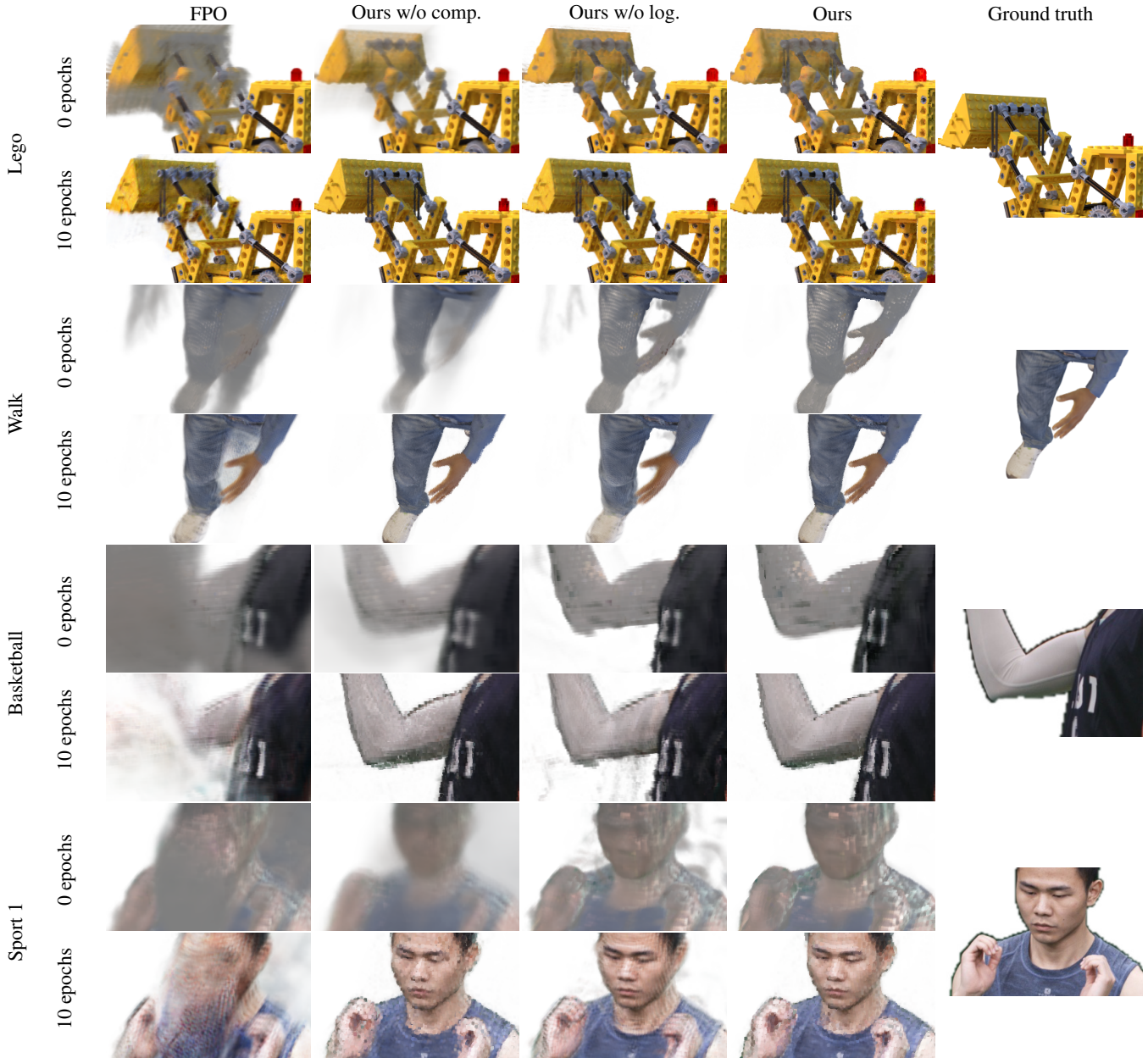


Figure 7: Visual comparison of the reconstructions of the three different scenes *Lego*, *Walk*, and *Basketball* with the logarithmic (log.) and component-dependent (comp.) encodings before and after fine-tuning for 10 epochs.

Since our proposed encoding only adds a few additional computation operations, its impact on the performance of the optimization and rendering is minimal. In fact, we still achieve real-time frame rates, as can be seen in Tab. 2 and the resulting FPS are even increased as space with former artifacts is now correctly identified as free space and skipped. Furthermore, our encoding does not change the required memory for storing an FPO, which on average is 2.8 GiB for the presented scenes. While the time step augmentation requires one additional flag to distinguish which time step

needs to be queried, the number of Fourier frequencies and, therefore, the number of entries per leaf stays the same.

#### 6.4. Ablation Studies

In Fig. 7, we present a more detailed overview of the effects of each part of our density encoding. Tab. 1 list the corresponding metrics for different scenes.

Especially the logarithmic part improves the reconstruction significantly, since the low frequency approximation can reconstruct

Table 2: Comparison of the frame rate averaged over all data sets with different combinations of logarithmic encoding (log.), component-dependent encoding (comp.) and time step augmentation (aug.), both before and after fine-tuning for 1 and 10 epochs. Best and second best results are marked in green and yellow, respectively.

Fine-tuning	0 epochs	1 epoch	10 epochs
FPO	70.897	79.991	88.539
Ours w/o comp.	50.868	76.089	94.732
Ours w/o log.	110.801	119.978	126.287
Ours	127.981	139.454	141.756
Ours with aug.	134.849	143.779	144.173

the functions of density much better than without it and most geometric artifacts are removed or become barely visible. The DFT and optimization process puts more attention to the reconstruction on lower values that require a smaller error for a good reconstruction.

The component-dependent part shows to be beneficial for a better initialization of the geometry reconstruction before fine-tuning. Gray artifacts are removed in most places at most time steps, as zero-densities are represented with negative values and are thus interpreted as free space. In combination with the logarithmic part, the quality of the initial geometry reconstruction is increased even further. After fine-tuning, the FPO initialized with only the component-depending part of the encoding achieves better results than the baseline FPO, but also in this case, our full encoding further improves the overall quality.

The time step augmentation aids in finding a better initial reconstruction of the geometry of the first and last time step as periodic artifacts are simply cut off, as we show in Fig. 8. While the augmentation improves the reconstruction of both time steps, the overall metrics are slightly worse than without augmentation. The reason for this is that the same amount of Fourier coefficients is used to compress  $T + 2$  instead of  $T$  time steps, which impairs the approximation for all time steps slightly. Without augmentation, all time steps are better approximated and the first and last time step, which are not reconstructed well, weigh less in the averaged metrics given in Tab. 1. Fig. 8 additionally shows the achieved PSNR values depending on the time step. After fine-tuning, the time step augmentation still improves the reconstruction as the optimization process is allowed to reconstruct arbitrary values at cut-off time steps and thus find a better reconstruction for the first and last time step.

Overall, each of the proposed strategies improves the reconstruction capabilities for the density of an FPO which, in turn, additionally accelerates the general rendering performance in terms of higher frame rates, see Tab. 2. They especially contribute towards a faithful initialization of the scene geometry, but also increase the quality of the reconstruction during fine-tuning compared to the original FPO approach.

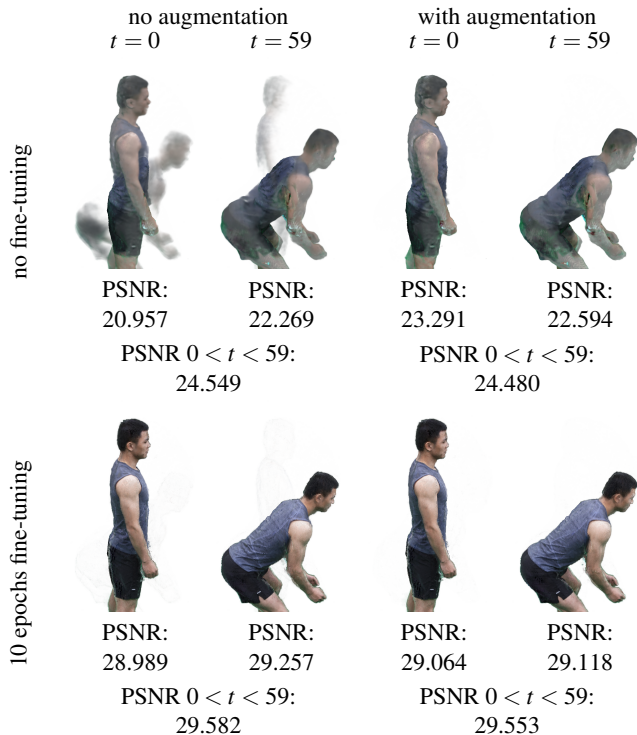


Figure 8: Visual comparison of the modified FPO for the *Sport 2* scene without and with time step augmentation for the first and last time step of the test sequence. PSNR values are averaged over all test views of the respective time step or time steps.

## 6.5. Limitations

Similar to other approaches, our method also has some limitations. The primary focus our encoding lies in transforming the density functions to make it easier to compress via the Fourier-based signal representation. SH coefficient functions, however, show different properties and are currently solely compressed using the DFT, which introduces similar artifacts as for the density function. While fine-tuning allows to improve the reconstruction, obtaining a realistic representation of the colors is also important and challenging problem. Furthermore, our methods inherits several limitations of the original FPO approach. Only the provided data is compressed, so generalization of the scene dynamics in terms of extrapolation and interpolation of the motion is not directly possible.

## 7. Conclusion

In this paper, we revisited Fourier PlenOctrees as an efficient representation for real-time rendering of dynamic Neural Radiance Fields and analyzed the characteristics of its compressed frequency-based representation. Based on the gained insights of the artifacts that are introduced by the compression in the context of the underlying volume rendering when state-of-the-art NeRF techniques are employed, we derived an efficient density encoding that counteracts these artifacts while retaining the compactness of FPOs and avoiding significant additional complexity or overhead. In combination with an additional data augmentation approach, our



method showed a superior reconstructed quality as well as a substantial further increase of the real-time rendering performance.

## Acknowledgments

This work has been funded by the Federal Ministry of Education and Research under grant no. 01IS22094E WEST-AI, by the Federal Ministry of Education and Research of Germany and the state of North-Rhine Westphalia as part of the Lamarr-Institute for Machine Learning and Artificial Intelligence, and additionally by the DFG project KL 1142/11-2 (DFG Research Unit FOR 2535 Anticipating Human Behavior).

## References

- [ALG\*21] ATTAL B., LAIDLAW E., GOKASLAN A., KIM C., RICHARDT C., TOMPKIN J., O'TOOLE M.: Törf: Time-of-flight radiance fields for dynamic scene view synthesis. *Advances in Neural Information Processing Systems (NeurIPS)* 34 (2021), 26289–26301. 2
- [BMT\*21] BARRON J. T., MILDENHALL B., TANCİK M., HEDMAN P., MARTIN-BRUALLA R., SRINIVASAN P. P.: Mip-nerf: A multiscale representation for anti-aliasing neural radiance fields. In *IEEE International Conference on Computer Vision (ICCV)* (2021), pp. 5855–5864. 2
- [BMV\*22] BARRON J. T., MILDENHALL B., VERBIN D., SRINIVASAN P. P., HEDMAN P.: Mip-nerf 360: Unbounded anti-aliased neural radiance fields. In *IEEE/CVF Conference on Computer Vision and Pattern Recognition (CVPR)* (2022), pp. 5470–5479. 2
- [BMV\*23] BARRON J. T., MILDENHALL B., VERBIN D., SRINIVASAN P. P., HEDMAN P.: Zip-nerf: Anti-aliased grid-based neural radiance fields. In *IEEE International Conference on Computer Vision (ICCV)* (2023). 2
- [BXS\*20] BI S., XU Z., SUNKAVALLI K., HAŠAN M., HOLDGEOFFROY Y., KRIEGMAN D., RAMAMOORTHY R.: Deep reflectance volumes: Relightable reconstructions from multi-view photometric images. In *European Conference on Computer Vision (ECCV)* (2020), Springer, pp. 294–311. 2
- [CCS\*15] COLLET A., CHUANG M., SWEENEY P., GILLET D., EYSEEV D., CALABRESE D., HOPPE H., KIRK A., SULLIVAN S.: High-quality streamable free-viewpoint video. *ACM Transactions on Graphics (TOG)* 34, 4 (2015), 1–13. 1
- [CFHT23] CHEN Z., FUNKHOUSER T., HEDMAN P., TAGLIASACCHI A.: Mobilenerf: Exploiting the polygon rasterization pipeline for efficient neural field rendering on mobile architectures. In *IEEE/CVF Conference on Computer Vision and Pattern Recognition (CVPR)* (2023), pp. 16569–16578. 1, 2
- [CJ23] CAO A., JOHNSON J.: Hexplane: A fast representation for dynamic scenes. In *IEEE/CVF Conference on Computer Vision and Pattern Recognition (CVPR)* (2023), pp. 130–141. 3
- [CMU22] CMU GRAPHICS LAB: Carnegie mellon university - cmu graphics lab - motion capture library, 2022. URL: <http://mocap.cs.cmu.edu/>. 6
- [CXG\*22] CHEN A., XU Z., GEIGER A., YU J., SU H.: Tensorf: Tensorial radiance fields. In *European Conference on Computer Vision (ECCV)* (2022), pp. 333–350. 2
- [DLZR22] DENG K., LIU A., ZHU J.-Y., RAMANAN D.: Depth-supervised nerf: Fewer views and faster training for free. In *IEEE/CVF Conference on Computer Vision and Pattern Recognition (CVPR)* (2022), pp. 12882–12891. 2
- [DZY\*21] DU Y., ZHANG Y., YU H.-X., TENENBAUM J. B., WU J.: Neural radiance flow for 4d view synthesis and video processing. In *IEEE International Conference on Computer Vision (ICCV)* (2021), IEEE Computer Society, pp. 14304–14314. 2
- [FKYT\*22] FRIDOVICH-KEIL S., YU A., TANCİK M., CHEN Q., RECHT B., KANAZAWA A.: Plenoxels: Radiance fields without neural networks. In *IEEE/CVF Conference on Computer Vision and Pattern Recognition (CVPR)* (2022), pp. 5501–5510. 2
- [FYW\*22] FANG J., YI T., WANG X., XIE L., ZHANG X., LIU W., NIESSNER M., TIAN Q.: Fast dynamic radiance fields with time-aware neural voxels. In *SIGGRAPH Asia Conference Papers* (2022), pp. 1–9. 2
- [GCD\*22] GUO X., CHEN G., DAI Y., YE X., SUN J., TAN X., DING E.: Neural deformable voxel grid for fast optimization of dynamic view synthesis. In *Asian Conference on Computer Vision (ACCV)* (2022), pp. 3757–3775. 1, 2
- [GKJ\*21] GARBIN S. J., KOWALSKI M., JOHNSON M., SHOTTON J., VALENTIN J.: Fastnerf: High-fidelity neural rendering at 200fps. In *IEEE International Conference on Computer Vision (ICCV)* (2021), pp. 14346–14355. 1, 2
- [GLD\*19] GUO K., LINCOLN P., DAVIDSON P., BUSCH J., YU X., WHALEN M., HARVEY G., ORTS-ESCOLANO S., PANDEY R., DOURGARIAN J., ET AL.: The relightables: Volumetric performance capture of humans with realistic relighting. *ACM Transactions on Graphics (TOG)* 38, 6 (2019), 1–19. 1
- [GSKH21] GAO C., SARAF A., KOPF J., HUANG J.-B.: Dynamic view synthesis from dynamic monocular video. In *IEEE International Conference on Computer Vision (ICCV)* (2021), pp. 5712–5721. 2
- [GTZN21] GAFNI G., THIES J., ZOLLHOFER M., NIESSNER M.: Dynamic neural radiance fields for monocular 4d facial avatar reconstruction. In *IEEE/CVF Conference on Computer Vision and Pattern Recognition (CVPR)* (2021), pp. 8649–8658. 2
- [HSM\*21] HEDMAN P., SRINIVASAN P. P., MILDENHALL B., BARRON J. T., DEBEVEC P.: Baking neural radiance fields for real-time view synthesis. In *IEEE International Conference on Computer Vision (ICCV)* (2021), pp. 5875–5884. 2
- [IRG\*23] IŞIK M., RÜNZ M., GEORGOPOULOS M., KHAKHULIN T., STARCK J., AGAPITO L., NIESSNER M.: Humanrf: High-fidelity neural radiance fields for humans in motion. *ACM Transactions on Graphics (TOG)* 42, 4 (2023), 1–12. 3
- [JMB22] JENA S., MULTON F., BOUKHAYMA A.: Neural mesh-based graphics. In *European Conference on Computer Vision Workshops (ECCVW)* (2022). 2
- [KIT\*21] KONDO N., IKEDA Y., TAGLIASACCHI A., MATSUO Y., OCHIAI Y., GU S. S.: Vaxnerf: Revisiting the classic for voxel-accelerated neural radiance field. *arXiv preprint arXiv:2111.13112* (2021). 2
- [KNL\*22] KURZ A., NEFF T., LV Z., ZOLLHÖFER M., STEINBERGER M.: Adanerf: Adaptive sampling for real-time rendering of neural radiance fields. In *European Conference on Computer Vision (ECCV)* (2022), pp. 254–270. 2
- [LCM\*22] LIU J.-W., CAO Y.-P., MAO W., ZHANG W., ZHANG D. J., KEPPO J., SHAN Y., QIE X., SHOU M. Z.: Devrf: Fast deformable voxel radiance fields for dynamic scenes. *Advances in Neural Information Processing Systems (NeurIPS)* 35 (2022), 36762–36775. 1, 2
- [LGZL\*20] LIU L., GU J., ZAW LIN K., CHUA T.-S., THEOBALT C.: Neural sparse voxel fields. *Advances in Neural Information Processing Systems (NeurIPS)* 33 (2020), 15651–15663. 2
- [LMTL21] LIN C.-H., MA W.-C., TORRALBA A., LUCEY S.: Barf: Bundle-adjusting neural radiance fields. In *IEEE International Conference on Computer Vision (ICCV)* (2021), pp. 5741–5751. 2
- [LMW21] LINDELL D. B., MARTEL J. N., WETZSTEIN G.: Autoint: Automatic integration for fast neural volume rendering. In *IEEE/CVF Conference on Computer Vision and Pattern Recognition (CVPR)* (2021), pp. 14556–14565. 2
- [LNSW21] LI Z., NIKLAUS S., SNAVELY N., WANG O.: Neural scene flow fields for space-time view synthesis of dynamic scenes. In *IEEE/CVF Conference on Computer Vision and Pattern Recognition (CVPR)* (2021), pp. 6498–6508. 2

- [LSS\*19] LOMBARDI S., SIMON T., SARAGIH J., SCHWARTZ G., LEHRMANN A., SHEIKH Y.: Neural volumes: learning dynamic renderable volumes from images. *ACM Transactions on Graphics (TOG)* 38, 4 (2019), 1–14. 2
- [LSS\*21] LOMBARDI S., SIMON T., SCHWARTZ G., ZOLLHOEFER M., SHEIKH Y., SARAGIH J.: Mixture of volumetric primitives for efficient neural rendering. *ACM Transactions on Graphics (TOG)* 40, 4 (2021), 1–13. 2
- [LSW\*22] LI L., SHEN Z., WANG Z., SHEN L., TAN P.: Streaming radiance fields for 3d video synthesis. *Advances in Neural Information Processing Systems (NeurIPS)* 35 (2022), 13485–13498. 2
- [LSZ\*22] LI T., SLAVCHEVA M., ZOLLHOEFER M., GREEN S., LASSNER C., KIM C., SCHMIDT T., LOVEGROVE S., GOESELE M., NEWCOMBE R., ET AL.: Neural 3d video synthesis from multi-view video. In *IEEE/CVF Conference on Computer Vision and Pattern Recognition (CVPR)* (2022), pp. 5521–5531. 1, 2, 6
- [LXL\*21] LIN K.-E., XIAO L., LIU F., YANG G., RAMAMOORTHY R.: Deep 3d mask volume for view synthesis of dynamic scenes. In *IEEE International Conference on Computer Vision (ICCV)* (2021), pp. 1749–1758. 2
- [Mak22] MAKEHUMAN: Makehuman - open source tool for making 3d characters, 2022. URL: [www.makehumancommunity.org](http://www.makehumancommunity.org). 6
- [MESK22] MÜLLER T., EVANS A., SCHIED C., KELLER A.: Instant neural graphics primitives with a multiresolution hash encoding. *ACM Transactions on Graphics (TOG)* 41, 4 (July 2022), 102:1–102:15. 1, 2, 6
- [MLL\*22] MA L., LI X., LIAO J., ZHANG Q., WANG X., WANG J., SANDER P. V.: Deblur-nerf: Neural radiance fields from blurry images. In *IEEE/CVF Conference on Computer Vision and Pattern Recognition (CVPR)* (2022), pp. 12861–12870. 2
- [MPH\*20] MEKA A., PANDEY R., HAENE C., ORTS-ESCOLANO S., BARNUM P., DAVID-SON P., ERICKSON D., ZHANG Y., TAYLOR J., BOUAZIZ S., ET AL.: Deep relightable textures: volumetric performance capture with neural rendering. *ACM Transactions on Graphics (TOG)* 39, 6 (2020), 1–21. 2
- [MSOC\*19] MILDENHALL B., SRINIVASAN P. P., ORTIZ-CAYON R., KALANTARI N. K., RAMAMOORTHY R., NG R., KAR A.: Local light field fusion: Practical view synthesis with prescriptive sampling guidelines. *ACM Transactions on Graphics (TOG)* 38, 4 (2019), 1–14. 2
- [MST\*20] MILDENHALL B., SRINIVASAN P., TANCIK M., BARRON J., RAMAMOORTHY R., NG R.: Nerf: Representing scenes as neural radiance fields for view synthesis. In *European Conference on Computer Vision (ECCV)* (2020). 1, 2, 6
- [NMOG20] NIEMEYER M., MESCHEDER L., OECHSLE M., GEIGER A.: Differentiable volumetric rendering: Learning implicit 3d representations without 3d supervision. In *IEEE/CVF Conference on Computer Vision and Pattern Recognition (CVPR)* (2020), pp. 3504–3515. 2
- [NSP\*21] NEFF T., STADLBAUER P., PARGER M., KURZ A., MUELLER J. H., CHAITANYA C. R. A., KAPLAYAN A., STEINBERGER M.: Donerf: Towards real-time rendering of compact neural radiance fields using depth oracle networks. *Computer Graphics Forum (CGF)* 40, 4 (2021), 45–59. 2
- [PCPMMN21] PUMAROLA A., CORONA E., PONS-MOLL G., MORENO-NOGUER F.: D-nerf: Neural radiance fields for dynamic scenes. In *IEEE/CVF Conference on Computer Vision and Pattern Recognition (CVPR)* (2021), pp. 10318–10327. 2
- [PSB\*21] PARK K., SINHA U., BARRON J. T., BOUAZIZ S., GOLDMAN D. B., SEITZ S. M., MARTIN-BRUALLA R.: Nerfies: Deformable neural radiance fields. In *IEEE International Conference on Computer Vision (ICCV)* (2021), pp. 5865–5874. 2
- [PZX\*21] PENG S., ZHANG Y., XU Y., WANG Q., SHUAI Q., BAO H., ZHOU X.: Neural body: Implicit neural representations with structured latent codes for novel view synthesis of dynamic humans. In *IEEE/CVF Conference on Computer Vision and Pattern Recognition (CVPR)* (2021), pp. 9054–9063. 2
- [RJY\*21] REBAIN D., JIANG W., YAZDANI S., LI K., YI K. M., TAGLIASACCHI A.: Derf: Decomposed radiance fields. In *IEEE/CVF Conference on Computer Vision and Pattern Recognition (CVPR)* (2021), pp. 14153–14161. 2
- [RPLG21] REISER C., PENG S., LIAO Y., GEIGER A.: Kilonerf: Speeding up neural radiance fields with thousands of tiny mlps. In *IEEE International Conference on Computer Vision (ICCV)* (2021), pp. 14335–14345. 2
- [SCL\*23] SONG L., CHEN A., LI Z., CHEN Z., CHEN L., YUAN J., XU Y., GEIGER A.: Nerfplayer: A streamable dynamic scene representation with decomposed neural radiance fields. *IEEE Transactions on Visualization and Computer Graphics* 29, 5 (2023), 2732–2742. 1, 2
- [SESM22] SUHAIL M., ESTEVES C., SIGAL L., MAKADIA A.: Light field neural rendering. In *IEEE/CVF Conference on Computer Vision and Pattern Recognition (CVPR)* (2022), pp. 8269–8279. 2
- [SSC22] SUN C., SUN M., CHEN H.-T.: Direct voxel grid optimization: Super-fast convergence for radiance fields reconstruction. In *IEEE/CVF Conference on Computer Vision and Pattern Recognition (CVPR)* (2022), pp. 5459–5469. 2
- [SZT\*23] SHAO R., ZHENG Z., TU H., LIU B., ZHANG H., LIU Y.: Tensor4d: Efficient neural 4d decomposition for high-fidelity dynamic reconstruction and rendering. In *IEEE/CVF Conference on Computer Vision and Pattern Recognition (CVPR)* (2023), pp. 16632–16642. 3
- [SZW19] SITZMANN V., ZOLLHÖFER M., WETZSTEIN G.: Scene representation networks: Continuous 3d-structure-aware neural scene representations. *Advances in Neural Information Processing Systems (NeurIPS)* 32 (2019). 2
- [TCY\*22] TANCIK M., CASSER V., YAN X., PRADHAN S., MILDENHALL B., SRINIVASAN P. P., BARRON J. T., KRETZSCHMAR H.: Block-nerf: Scalable large scene neural view synthesis. In *IEEE/CVF Conference on Computer Vision and Pattern Recognition (CVPR)* (2022), pp. 8248–8258. 2
- [TMW\*21] TANCIK M., MILDENHALL B., WANG T., SCHMIDT D., SRINIVASAN P. P., BARRON J. T., NG R.: Learned initializations for optimizing coordinate-based neural representations. In *IEEE/CVF Conference on Computer Vision and Pattern Recognition (CVPR)* (2021), pp. 2846–2855. 2
- [TTG\*21] TRETSCHK E., TEWARI A., GOLYANIK V., ZOLLHÖFER M., LASSNER C., THEOBALT C.: Non-rigid neural radiance fields: Reconstruction and novel view synthesis of a dynamic scene from monocular video. In *IEEE International Conference on Computer Vision (ICCV)* (2021), pp. 12959–12970. 2
- [WBSS04] WANG Z., BOVIK A. C., SHEIKH H. R., SIMONCELLI E. P.: Image quality assessment: from error visibility to structural similarity. *IEEE Transactions on Image Processing (TIP)* 13, 4 (2004), 600–612. 7
- [WCS\*22] WENG C.-Y., CURLESS B., SRINIVASAN P. P., BARRON J. T., KEMELMACHER-SHLIZERMAN I.: Humannerf: Free-viewpoint rendering of moving people from monocular video. In *IEEE/CVF Conference on Computer Vision and Pattern Recognition (CVPR)* (2022), pp. 16210–16220. 2
- [WHH\*23] WANG L., HU Q., HE Q., WANG Z., YU J., TUYTELAARS T., XU L., WU M.: Neural residual radiance fields for streamably free-viewpoint videos. In *IEEE/CVF Conference on Computer Vision and Pattern Recognition (CVPR)* (2023), pp. 76–87. 2
- [WLB\*22] WU L., LEE J. Y., BHATTAD A., WANG Y.-X., FORSYTH D.: Diver: Real-time and accurate neural radiance fields with deterministic integration for volume rendering. In *IEEE/CVF Conference on Computer Vision and Pattern Recognition (CVPR)* (2022), pp. 16200–16209. 2
- [WSR\*23] WANG S., SUPIKOV A., RATCLIFF J., FUCHS H., AZUMA R.: Inv: Towards streaming incremental neural videos. *arXiv preprint arXiv:2302.01532* (2023). 6
- [WWG\*21] WANG Q., WANG Z., GENOVA K., SRINIVASAN P. P., ZHOU H., BARRON J. T., MARTIN-BRUALLA R., SNAVELY N.,

- FUNKHOUSER T.: Ibrnet: Learning multi-view image-based rendering. In *IEEE/CVF Conference on Computer Vision and Pattern Recognition (CVPR)* (2021), pp. 4690–4699. [1](#)
- [WWHY20] WU M., WANG Y., HU Q., YU J.: Multi-view neural human rendering. In *IEEE/CVF Conference on Computer Vision and Pattern Recognition (CVPR)* (2020), pp. 1682–1691. [2](#), [6](#)
- [WWL\*21] WANG L., WANG Z., LIN P., JIANG Y., SUO X., WU M., XU L., YU J.: ibutter: Neural interactive bullet time generator for human free-viewpoint rendering. In *ACM International Conference on Multimedia* (2021), pp. 4641–4650. [2](#)
- [WWX\*21] WANG Z., WU S., XIE W., CHEN M., PRISACARIU V. A.: Nerf--: Neural radiance fields without known camera parameters. *arXiv preprint arXiv:2102.07064* (2021). [2](#)
- [WZL\*22] WANG L., ZHANG J., LIU X., ZHAO F., ZHANG Y., ZHANG Y., WU M., YU J., XU L.: Fourier plenotrees for dynamic radiance field rendering in real-time. In *IEEE/CVF Conference on Computer Vision and Pattern Recognition (CVPR)* (2022), pp. 13524–13534. [1](#), [3](#), [6](#)
- [WZML23] WANG P., ZHAO L., MA R., LIU P.: Bad-nerf: Bundle adjusted deblur neural radiance fields. In *IEEE/CVF Conference on Computer Vision and Pattern Recognition (CVPR)* (June 2023), pp. 4170–4179. [2](#)
- [XAS21] XU H., ALLDIECK T., SMINCHISESCU C.: H-nerf: Neural radiance fields for rendering and temporal reconstruction of humans in motion. *Advances in Neural Information Processing Systems (NeurIPS)* 34 (2021), 14955–14966. [2](#)
- [YGLK21] YARIV L., GU J., KASTEN Y., LIPMAN Y.: Volume rendering of neural implicit surfaces. *Advances in Neural Information Processing Systems (NeurIPS)* 34 (2021), 4805–4815. [2](#)
- [YKM\*20] YARIV L., KASTEN Y., MORAN D., GALUN M., ATZMON M., RONEN B., LIPMAN Y.: Multiview neural surface reconstruction by disentangling geometry and appearance. *Advances in Neural Information Processing Systems (NeurIPS)* 33 (2020), 2492–2502. [2](#)
- [YLT\*21] YU A., LI R., TANCIK M., LI H., NG R., KANAZAWA A.: Plenotrees for real-time rendering of neural radiance fields. In *IEEE International Conference on Computer Vision (ICCV)* (2021), pp. 5752–5761. [1](#), [2](#), [3](#), [6](#)
- [ZIE\*18] ZHANG R., ISOLA P., EFROS A. A., SHECHTMAN E., WANG O.: The unreasonable effectiveness of deep features as a perceptual metric. In *IEEE/CVF Conference on Computer Vision and Pattern Recognition (CVPR)* (2018), pp. 586–595. [7](#)
- [ZLY\*21] ZHANG J., LIU X., YE X., ZHAO F., ZHANG Y., WU M., ZHANG Y., XU L., YU J.: Editable free-viewpoint video using a layered neural representation. *ACM Transactions on Graphics (TOG)* 40, 4 (2021), 1–18. [2](#)
- [ZRSK20] ZHANG K., RIEGLER G., SNAVELY N., KOLTUN V.: Nerf++: Analyzing and improving neural radiance fields. *arXiv preprint arXiv:2010.07492* (2020). [2](#)